State-Plane Centric Control of Bidirectional Dual Active Bridge Converters in V2X Applications

Matteo Sposito, *Graduate Student Member, IEEE*, and Ignacio Galiano Zurbriggen, *Member, IEEE*

***Abstract*—Dual active bridge (DAB) converters are a common choice for bidirectional battery chargers due to their efficient dc–dc isolation capabilities and the possibility to control power flow direction. The control of this topology using traditional linear controllers based on small-signal models typically leads to a slower dynamic response, especially during large transients. This article introduces a novel state-plane centric pulsewidth modulation controller for DAB converters, enabling fast and reliable large transient response while ensuring robustness to parameter variations and loss estimation inaccuracies. This study introduces a state-plane model of the DAB converter employing single-phase-shift modulation and the large-signal dynamics of the output *LC* filter. The state-plane model is defined by circular trajectories, with centers determined by the operating conditions and control variables. Based on this model, a controller with fast and predictable large transient dynamics is derived, with no overshoots, oscillations, or spikes, which helps reduce battery degradation. The proposed control is suitable for implementation using industry-standard sensing and digital control solutions, offering a promising solution for efficient and reliable power conversion in ON-board and OFF-board charging applications, and despite the geometric formulation, it maintains low implementation complexity. Comprehensive and detailed mathematical procedures reinforce the theoretical concepts, and the controller's implementation is validated through experimental results.**

***Index Terms*—Dual active bridge (DAB), fast dynamics, state-plane centric control, vehicle-to-everything (V2X).**

I. Introduction

DUAL active bridge (DAB) converters are widely used in bidirectional battery chargers [1], solid-state transformers [2], and low- to medium-voltage grid applications [3] due to their high-frequency galvanic isolation and soft switching. Several aspects of the DAB converters, including topology, design, modulation, and efficiency improvements, have been detailed in [4], [5], [6], [7], and different modulation techniques, along with a combined approach between them and variable switching frequency, are presented in [8]. Other variations of this topology can be used to increase power, such as the three-phase DAB presented in [9], [10]. In addition, efficiency improvements can be achieved by incorporating resonance between the two full bridges, as seen in the *CLLC* converter [11]. Furthermore, switching stress can be reduced using a multilevel topology, as discussed in [12] and [13]. Using small-signal-based controllers for DAB converters can be used for common applications such as fast chargers [14], [15] due to their robustness, but they can lead to poor large transient dynamic performance. Various nonlinear control strategies have been proposed to improve the converter's large-signal behavior, including sliding-mode control [16], [17], passivity-based control [18], model predictive control [19], [20], [21], and natural switching surfaces [22]. The large-signal stability of the DAB is approached using state trajectories on the transformer side in [23], as well as the fast dynamic response [24] and soft start-up methods to improve soft-switching operation and minimize inrush currents [25]. While effective, these methods require higher implementation complexity (i.e., higher sensing bandwidth and computational power) compared to industry-standard solutions. A pulsewidth modulation (PWM)-based average state-plane control approach for fundamental dc–dc converters that achieve a smooth and reliable response while maintaining industry-standard implementation was introduced in [26], a similar approach for flyback converters is detailed in [27], while a dual-loop geometric approach that combines a nonlinear state-plane-based outer voltage loop with feedback linearization and a linear controller for the inner current loop was introduced in [28]. Following a similar state-plane-based approach, this work introduces a state-plane centric control for DAB-based battery chargers [see in Fig. 1(a)] to achieve ultrafast large transient performance while maintaining low implementation requirements. The proposed solution is particularly effective in applications such as vehicle-to-grid (V2G) and vehicle-to-home, also known as vehicle-to-everything (V2X), illustrated in Fig. 1(b), which require a fast large transient response to transition between operating modes seamlessly and without interrupting the power. The proposed method enables full control over the transient response for any operating point and system parameters, avoiding undesired spikes in the battery current during large transients. The proposed technique is simple to implement and it shows low sensing bandwidth and computational power requirements, ensuring that the state-plane centric control can be implemented using industry-standard microcontrollers, with no need for high-resolution analog-to-digital converters (ADCs), high-bandwidth sensors, or complex controllers, making it highly suitable for industrial applications.

Received 20 December 2024; revised 24 March 2025 and 29 May 2025; accepted 10 July 2025. Date of publication 23 July 2025; date of current version 8 September 2025. Recommended for publication by Associate Editor D. M. Xu. *(Corresponding author: Ignacio Galiano Zurbriggen.)*

Matteo Sposito is with the Department of Electrical and Software Engineering, University of Calgary, Calgary, AB T2N 1N4, Canada (e-mail: matteo.sposito@ieee.org).

Ignacio Galiano Zurbriggen is with the School of Sustainable Energy Engineering, Simon Fraser University, Vancouver, BC V6B 5K3, Canada (e-mail: igaliano@ieee.org).

Color versions of one or more figures in this article are available at https://doi.org/10.1109/TPEL.2025.3592112.

Digital Object Identifier 10.1109/TPEL.2025.3592112

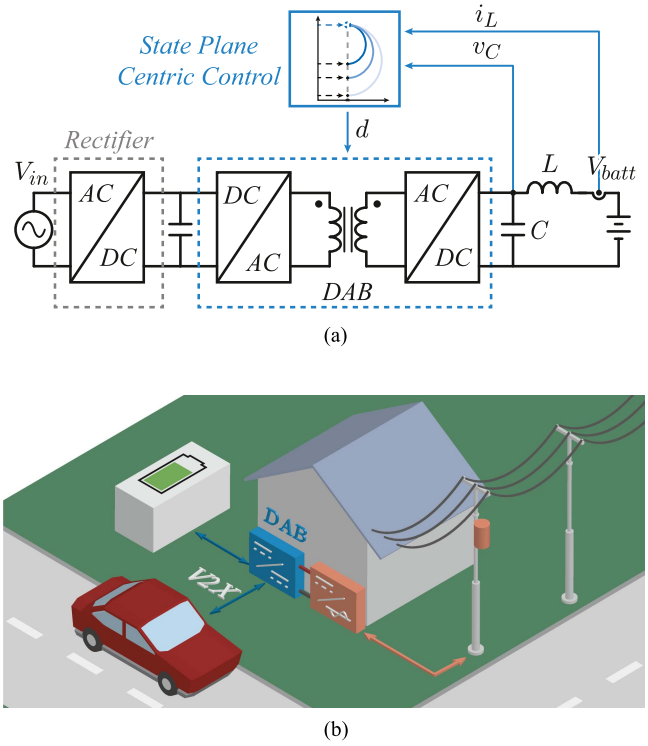

Fig. 1. (a) State-plane centric control architecture of the output current for a DAB converter connected to an active rectifier for a bidirectional recharging station. (b) Representation of a V2X architecture involving the battery of a vehicle, a static battery, and the grid-connected battery recharging station.

A preliminary and unidirectional version of the state-plane centric control for DAB-based battery chargers proposed in this work was presented as a conference paper in 2024 IEEE Energy Conversion Congress and Exposition [29]. This article presents an extended model that accounts for leakage inductor losses, transformer resistive effects, and losses in the battery and output *LC* tank. In addition, it extends the analysis, to include the average model of the rectified current in both charging and discharging operating modes and an output resistance estimation algorithm. The combination of the state-plane centric control and the output losses estimation enables an ultrafast transient response and a stable steady-state conditions, in different operation mode (G2V or V2G) and considering different state of charge (SOC). Unlike other approaches, the proposed state-plane centric control method directly leverages the large-signal behavior of the DAB converter, ensuring fast and predictable transients without requiring high-bandwidth sensing, variable switching frequency, or complex optimization routines. This results in a control strategy that is both computationally efficient and robust to real-world applications. The proposed method is thoroughly validated through extensive simulation and experimental results for positive and negative output currents as well as the emulation of a grid malfunction.

II. DAB Modeling

The DAB converter is shown in Fig. 2(a) and its control variable, the phase shift between the primary and the secondary

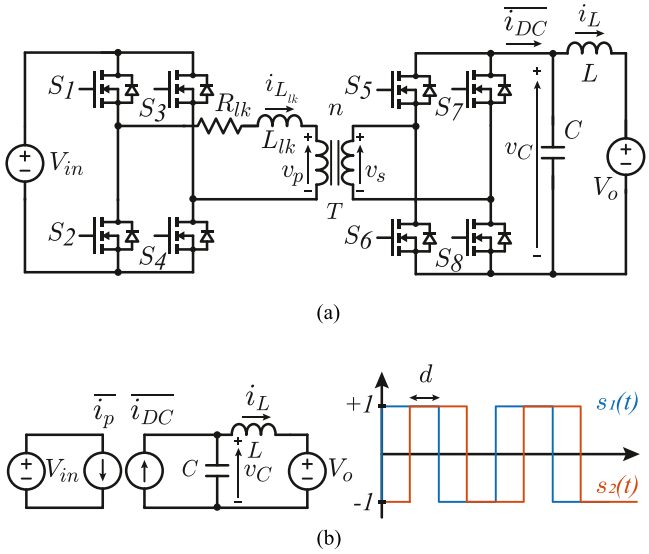

Fig. 2. (a) Model of a DAB Converter indicating leakage inductor current $i_{L_{lk}}$ and i_L the battery charging/discharging current. (b) Average model of the DAB with an output LC filter.

bridge, can be defined as an angle ϕ, and the value is defined in the interval $[-180°, 180°]$ or in per unit, defined as d and in the interval $[-1, 1]$. Using single-phase-shift modulation and defining the value of the phase shift as d, the power flow can be controlled by adjusting it between the primary and the secondary switch signals $s_1(t)$ and $s_2(t)$, as illustrated in Fig. 2(b) and according to the following equations:

$$s_1(t) = \begin{cases} 1, & 0 \le t < \frac{T_{sw}}{2} \\ -1, & \frac{T_{sw}}{2} \le t < T_{sw} \end{cases} \tag{1}$$

$$s_2(t) = \begin{cases} 1, & \frac{dT_{sw}}{2} \le t < \frac{T_{sw}}{2} + \frac{dT_{sw}}{2} \\ -1, & 0 \le t < \frac{dT_{sw}}{2} \text{ or } \frac{T_{sw}}{2} + \frac{dT_{sw}}{2} \le t < T_{sw}. \end{cases} \tag{2}$$

When the power switches S_1 and S_4 are turned ON, $s_1(t) = 1$; conversely, when power switches S_2 and S_3 are turned ON, $s_1(t) = -1$. Similarly, when power switches S_5 and S_8 are activated, $s_2(t) = 1$, and when S_6 and S_7 are turned ON, $s_1(t) = -1$. The leakage inductor current $i_{L_{lk}}$ direction depends on the switching state of the power switches, leading to the classification of states into six categories in the analysis, due to the current direction. However, as certain circuit state variables remain constant between specific stages, the mathematical model calculation for the DAB converter's steady-state power can be broken down into four stages.

A. Converter's Average Model

The modulation used to control the power flow of the DAB has an impact on the derivation of the final model. The dynamics of the total inductance, which is composed by the leakage inductance and the transformer's one, represented in this work as ($i_{L_{lk}}$), and output voltage (v_C) of the single-phase-shifted-modulated DAB converter can be mathematically described using the switch control signals introduced in (1) and (2) combined

with the common differential equations

$$L\frac{di_{L_{\text{lk}}}}{dt} = s_1(t)\ V_{\text{in}} - n\ s_2(t)\ v_C - R_{L_{\text{lk}}}\ i_{L_{\text{lk}}} \tag{3}$$

$$C\frac{dv_C}{dt} = n\ s_2(t)\ i_{L_{\text{lk}}} - i_o \tag{4}$$

where v_C is the voltage across the output capacitor, while the current i_o is the charging/discharging current of it, and n is the transformer turn ratio and $R_{L_{\text{lk}}}$ is the sum of the losses between the two H-bridges, represented as a resistor in series with the leakage inductor. By employing (3) and (4), and avoiding the effects of $R_{L_{\text{lk}}}$, the average value of the secondary-side rectified current can be expressed considering the peak values of the leakage inductor current described in Fig. 6(b)

$$i_{L1_{Lk}} = \frac{v_C - n\ V_{\text{in}} + 2\ n\ d\ V_{\text{in}}}{4\ n\ L_{\text{lk}} f_{\text{sw}}} \tag{5}$$

$$i_{L2_{Lk}} = \frac{2\ d\ v_C + n\ V_{\text{in}} - v_C}{4\ n\ L_{\text{lk}} f_{\text{sw}}}. \tag{6}$$

Using these expressions, and considering the total switching period $t_{\text{sw}} = t_1 + t_2 + (1-d)\ t_{\text{sw}}$ the instantaneous value of the average rectified current on the secondary side can be simplified, resulting in

$$\overline{i_{\text{DC}}} = n\ i_{L_{\text{lk}}}\ s_2(t) = \frac{V_{\text{in}}\ d(1-d)}{2\ n\ f_{\text{sw}}\ L_{\text{lk}}}. \tag{7}$$

The aforementioned equation simplifies the DAB model neglecting high-frequency dynamics, including semiconductor switching losses (soft and hard switching) and parasitic losses in passive components. While these factors influence the converter's performance, they primarily affect steady-state behavior rather than transient dynamics. The proposed state-plane centric control method compensates for these unmodeled effects by dynamically adjusting the control variables based on real-time measurements, ensuring fast and accurate transient performance despite the model simplifications.

B. Output Dynamics Average Model

The dynamic behavior at the DAB converter's output port is described by the differential equations of the LC tank illustrated in Fig. 2(b). Normalizing the system behavior using the LC characteristic impedance ($Z_0 = \sqrt{LC}$), the LC resonant period ($T_0 = 2\pi\sqrt{LC}$), and the nominal output voltage (V_{o_n}) as base quantities ensures generality. The resulting normalized structure is independent of the converter voltage and current levels as well as the LC circuit parameters.

$$\frac{1}{2\pi}\frac{di_{L_n}}{dt_n} = v_{C_n} - V_{o_n} \tag{8}$$

$$\frac{1}{2\pi}\frac{dv_{C_n}}{dt_n} = \overline{i_{\text{DC}_n}} - i_{L_n} \tag{9}$$

where X_n represents the normalized quantities. The time evolution of the state variables can be obtained by solving (8) and (9) yielding sinusoidal waveforms, as illustrated in Fig. 3. Combining the solutions in the state-plane formed by the output filter capacitor voltage v_{C_n} and inductor current i_{L_n}, the evolution of

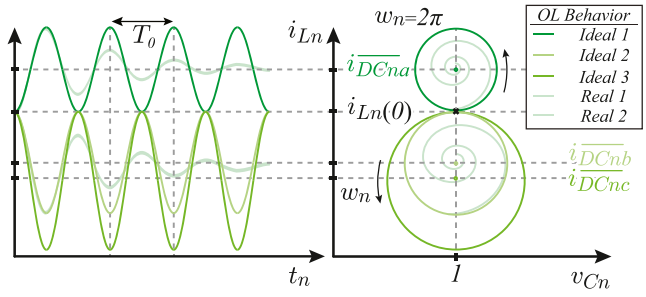

Fig. 3. DAB converter time response and state-plane evolution in terms of inductor current i_L, average rectified current $\overline{i_{\text{DC}}}$, and phase shift d in normalized open loop.

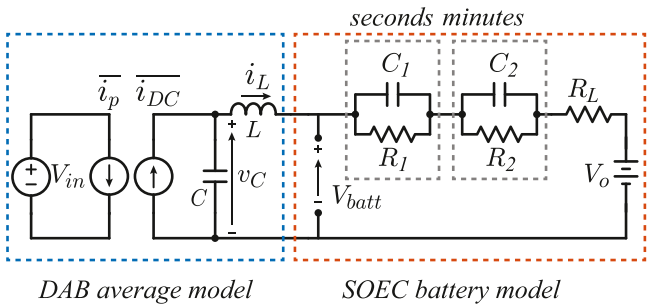

Fig. 4. DAB converter average model combining the output LC tank and the battery SOEC model.

the operating point can be characterized by circular trajectories (see Fig. 3), with center coordinates $[V_{o_n} = 1, \overline{i_{\text{DC}_n}}]$, and initial conditions $[V_{o_n} = 1, i_{L_n}(0)]$

$$\left(i_{L_n} - \overline{i_{\text{DC}_n}}\right)^2 + \left(v_{C_n} - V_{o_n}\right)^2 = \left(i_{L_n}(0) - \overline{i_{\text{DC}_n}}\right)^2 + \left(v_{C_n}(0) - V_{o_n}\right)^2. \tag{10}$$

In the normalized domain

$$\left(i_{L_n} - \overline{i_{\text{DC}_n}}\right)^2 + \left(v_{C_n} - 1\right)^2 = \left(i_{L_n}(0) - \overline{i_{\text{DC}_n}}\right)^2 + \left(v_{C_n}(0) - 1\right)^2. \tag{11}$$

By adjusting $\overline{i_{\text{DC}}}$, the center displacement can be calculated to achieve the desired state-plane trajectory from any initial conditions. In the ideal case, without losses, the final capacitor voltage value equals the initial one and matches the output-normalized voltage, considering the output load as an ideal voltage source. Still, in the real case, v_C has a displacement due to the losses embedded in the output tank and the series resistance of the battery.

C. Battery Average Model

The model described in Section II-B involves an ideal output voltage source, but a more detailed model can be developed involving the accurate model of the battery and its losses. This last introduces damping effects, which lead to spiral trajectories in the state-plane domain and decaying sinusoidal waveforms in the time domain as shown in Fig. 3. To model the battery, the second-order equivalent circuit (SOEC) shown in Fig. 4 is used, where the V_o represents the open-circuit voltage, which depends

on the battery SOC, the R_L is the battery internal resistance, and the two parallel RC circuits represent the slow and fast time constants. These parameters are functions of the time τ, and the charging/discharging current i_L, the equation that describes the SOEC battery model is the following:

$$V_{\text{batt}}(\tau) = V_o + i_L(\tau)R_L + i_L R_1\left(1 - e^{-\frac{\tau}{\tau_1}}\right) + i_L(\tau)R_2\left(1 - e^{\frac{\tau}{\tau_2}}\right) \tag{12}$$

where $V_{\text{batt}}(\tau)$ is the terminal voltage of the battery, and the time constants τ_1 and τ_2 are determined by the two RC networks, and the current $i_L(\tau)$ represents the charging or discharging current. Considering the fast dynamics of the state-plane centric control discussed in this work, the RC networks, which typically operate in the second or minutes range, can be approximated as short circuits. As a result, the battery dynamics simplify to the voltage drop across the resistance R_L and the open-circuit voltage V_o.

III. Closed-Loop State-Plane Centric Control

A. Target-Approaching Trajectories

As detailed in Section II, the center of the circular trajectories can be adjusted by modifying the average value of the secondary side rectified current $\overline{i_{\text{DC}}}$. Therefore, starting from any initial conditions $[v_{C_n}(0), i_{L_n}(0)]$, a unique circular trajectory can be followed to reach the target operating point $[V_{\text{batt}_n}, i_{L_{nt}}]$. The geometric approach ensures that transients to follow a unique circular trajectory rather than a stepwise or oscillatory transition. This circle can be found by inserting the target operating point into (10)

$$\left(i_{L_{nt}} - \overline{i_{\text{DC}}}\right)^2 - \left(i_{L_n}(0) - \overline{i_{\text{DC}}}\right)^2 + \left(v_{C_n} - V_{\text{batt}_n}\right)^2 = 0. \tag{13}$$

Given that the values of v_{C_n} and i_{L_n} measured during each switching cycle, the algorithm can update v_{C_n} and i_{L_n} once per switching cycle. This allows the controller to adjust the center of the circular trajectory accordingly and compensate for potential deviations due to unmodeled behaviors to achieve the desired final value as quickly as possible. Using (13), the value of the averaged rectified current $\overline{i_{\text{DC}_x}}$ needed to follow the desired unique circular trajectory can be written as follows:

$$\overline{i_{\text{DC}_x}} = \left[\frac{{i_{L_{nt}}}^2 - {i_{L_n}}^2 - \left(v_{C_n} - V_{\text{batt}_n}\right)^2}{2\left(i_{L_{nt}} - i_{L_n}\right)}\right]. \tag{14}$$

The time-domain and state-plane plots shown in Fig. 5 illustrate how starting from any initial conditions for both i_{L_n} and v_C, the average current $\overline{i_{\text{DCx}}}$ can be adjusted to reach the target point following a unique circular trajectory in both directions, enabling the DAB to work in charging and discharging mode. Unlike traditional and industry-standard methods, this method uses a trajectory planning approach, which prevents overshoot, chattering phenomena or spikes in both output current and voltage. The phase shift (d) required to obtain the desired $\overline{i_{\text{DC}x}}$

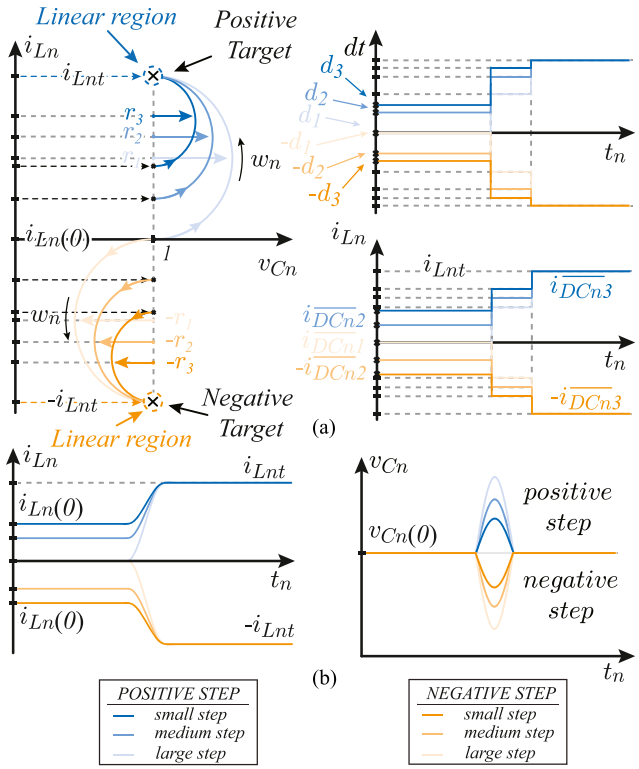

Fig. 5. DAB converter time response and state-plane evolution in terms of inductor current i_L, average rectified current $\overline{i_{\text{DC}}}$, and phase shift d in normalized closed loop. (a) State-plane and time domain control variables. (b) Statevariablesin time domain.

can be calculated using

$$d = \frac{1}{2} \pm \sqrt{\frac{1}{4} - \left(\frac{\overline{i_{\text{DC}_x}}\ 2\ n\ f_{\text{sw}}\ L_{\text{lk}}}{V_{\text{in}}}\right)}. \tag{15}$$

The phase-shift variable d is constrained to be in $[-0.5, 0.5]$ by the control algorithm. The positive values are related to the electric vehicle (EV) charging mode while the negative ones are related to the V2X mode. While the model used to derive (14) and (15) does not explicitly account for switching and passive component losses, the proposed control method inherently compensates for these factors. The proposed control algorithm uses a nonlinear controller for transients that relies on real-time measurement of the v_C and i_L, updating the operating point every switching cycle, and integrates it with a slow compensator to maintain the phase shift at the target point, as a result, any deviations caused by unmodeled losses are automatically corrected during operation, ensuring that the desired transient response remains unaffected. When the operating point is sufficiently close to the target, the output current gets into the linear region, which is a final circle defined by the controller in the neighborhood of the target point, as shown in Fig. 5(a), and the slow integrator is incorporated into the calculation of the final phase shift, allowing the state-plane centric control to achieve and maintain the desired output current, keeping it constant until further changes occur without compromising the fast transient calculation.

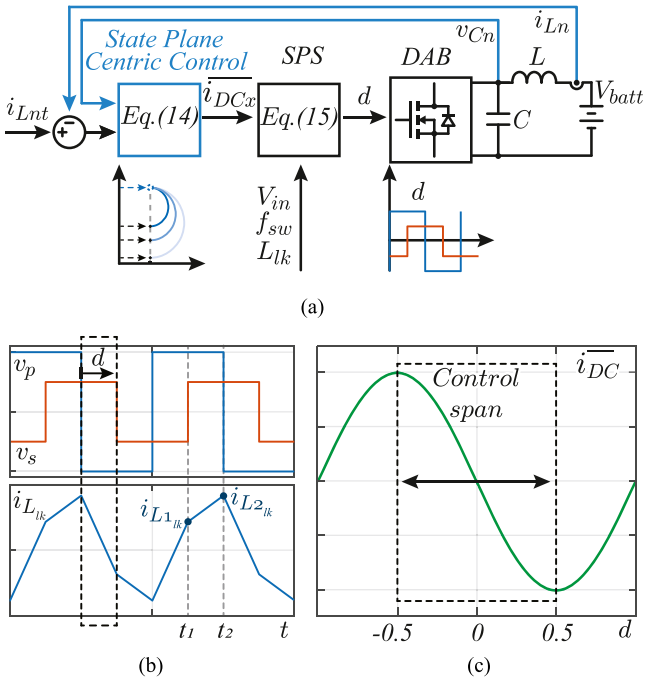

Fig. 6. (a) State-plane centric control using an output LC filter and with no losses. (b) Simulation of transformers waveforms of primary- and secondary-side voltages and leakage inductor current $i_{L_{lk}}$ with $d = 0.5$. (c) Power output with respect to the value of the phase shift d.

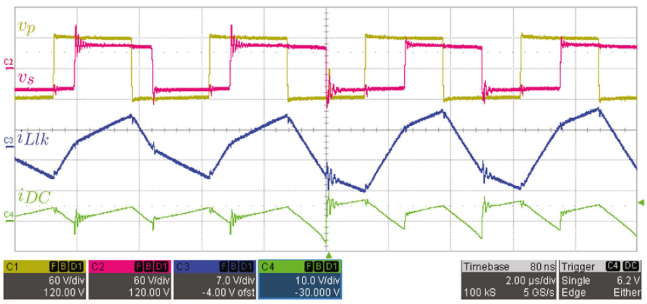

Fig. 7. Open-loop experimental results of the transformer waveforms of primary- and secondary-side voltages, leakage inductor current $i_{L_{lk}}$, and secondary side rectified current i_{DC} with a positive step, leading to the maximum charging current.

B. Implementation

The implementation of the complete diagram of the DAB battery charger state-plane centric control is shown in Fig. 8, and the detailed mathematical implementation without the losses compensator in shown in Fig. 6(a), which explains how the center of the output circular trajectory is calculated every switching cycle even if the value on v_{Cn} is unknown, leading to a rapid control but with a steady-state error. The battery inductor current i_{L_n} and the capacitor voltage v_{C_n} are measured once per PWM cycle. Based on the measurements, the desired average rectified current value ($\overline{i_{DCx}}$) is calculated every switching cycle using (14), which ensures the controller can dynamically adapt to changes in current and voltage, actively compensating for unmodeled dynamics. The center of the circular trajectory ($\overline{i_{DCx}}$, v_C) is adjusted based on the measured values of the capacitor voltage and the output inductor current. Although the voltage

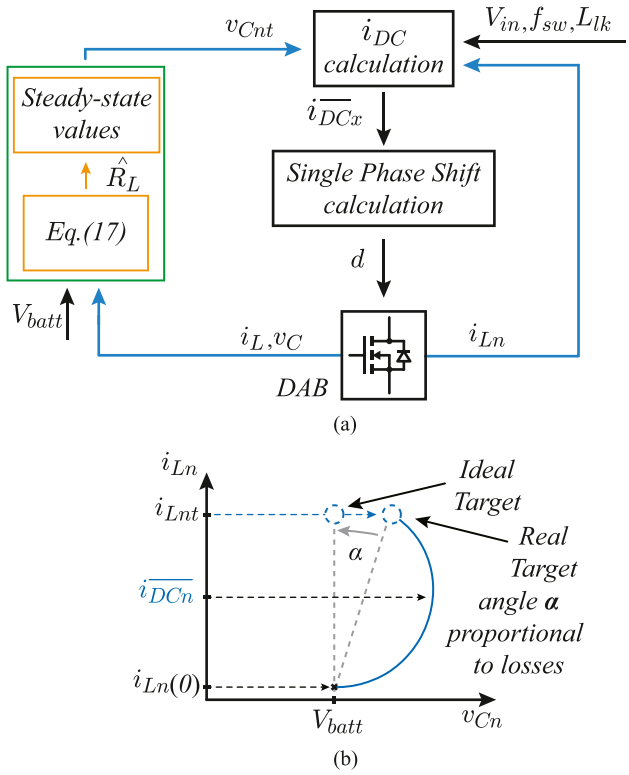

Fig. 8. (a) State-plane centric control complete scheme including the output losses estimation algorithm. (b) State-plane interpretation of the compensator.

displacement is significantly smaller than the current displacement, this value plays a crucial role in adjusting the center to achieve steady-state conditions in the normalized domain. The final average natural trajectory is a positive counterclockwise circle when the controller applies the positive step and a negative counterclockwise circle with a negative one. Then, the required phase-shift value d is calculated using (15) and applied to shift the secondary full bridge with respect to the primary side full bridge. The operational span of the control action is constrained to $d \in [-0.5, 0.5]$, to ensure a monotonic behavior on the i_{DC} versus d curve [shown in Fig. 6(c)], and obtain maximum charge/discharge currents for the extreme values of d and to be able to control the power flow accordingly, considering that the maximum current is limited by the total inductance between the two bridges (including both the transformer and leakage inductance). All the real-time computations are based on simple algebraic expressions and require few mathematical operations per switching cycle. These operations, computed at 200 kHz, do not require high processing power, and can be executed on a standard 32-bit microcontroller. In the state-plane domain, the capacitor voltage has a displacement between its initial and final values in both positive and negative steps. This displacement is caused by the series losses R_L, which includes battery resistance and inductance. As shown in Fig. 8(b), this displacement is proportional to it.

C. Output Losses Estimation

The final phase shift required to achieve the target point within the linear region, and thus maintain steady-state equilibrium, is

determined by (15). However, directly setting the final value of d fails to account for the losses effects. The R_L parameter, included in the DAB circuit and in series with L, represents the combined losses of the FETs, the transformer, and output losses. To address this issue, a slow integrator is implemented to estimate output losses, enabling correction and stabilization of the final value at the desired steady-state conditions. The value of the resistor must be included in the v_C calculation, as illustrated in Fig. 8 The integrator was designed to be at least 20 times slower than the state-plane centric control, operating only on the steady-state current regulation error. Its purpose is to compensate for losses by adding a small correction term to the ideal average rectified current in steady state calculated by the state-plane centric control. Specifically, the final value is given by

$$\overline{i_{\mathrm{DC_{ss}}}} = \left[\frac{{i_{L_{nt}}}^2 - {i_{L_n}}^2 - (v_{C_{nt}} - 1)^2}{2\,(i_{L_{nt}} - i_{L_n})}\right] \tag{16}$$

where $i_{\mathrm{DC_{ss}}}$ is adjusted just in steady state, and the $v_{C_{nt}}$ term is a loss-compensating voltage drop calculated considering $\hat{R}_L$. The integrator time constant is deliberately chosen to be significantly slower than the state-plane centric control control dynamics ($K_{\mathrm{int}} \ll 1$) to avoid interfering with the transient performance shaped by the main controller. The calculation of $\hat{R}_L$ is given by

$$\hat{R}_L \approx K_{\mathrm{int}} \int_0^T \frac{e_i(t)}{v_C(0)} dt = K_{\mathrm{int}} \int_0^T (\alpha(t))\, dt \tag{17}$$

where $\hat{R}_L$ is the estimation value of the overall output losses, and $e_i(t)$ is the output current error $(i_{L_{nt}} - i_{L_n})$. The integrator was tuned using the pole-zero cancellation, where $\hat{R}_L$ is the estimation value of the overall output losses. As $\hat{R}_L$ converges toward the actual value of R_L, the zero introduced by the compensator aligns with the pole of the plant at $-R_L/L$, enabling the cancellation of the resistive dynamics. The slow integral compensator mitigates steady-state deviations without affecting transient performance. Even small errors, such as incorrect initial conditions in the loss estimation (see Fig. 10), do not affect the fast transient dynamics, however, they do impact steady-state conditions. To compensate for this, an integral term is added to the control, ensuring automatic error correction over time.

IV. Simulations Results

The simulation results of the DAB-based battery charger, using the parameter values detailed in Table I, are shown in Figs. 6(b) and 9. In particular, Fig. 6(b) illustrates the final phase shift achieved by the converter during charging mode with a positive current step. System values of $V_{\mathrm{in}} = 800$ V and $V_{\mathrm{batt}} = 500$ V, as well as $P_{\mathrm{out}} = 25$ kW and $I_L = 50$ A were chosen to reflect common automotive applications, while L_{lk} and f_{sw} were selected based on the power requirements. In Fig. 9(a) and (b), the output current simulation shows a positive step from $i_{L_n}(0)$ to $i_{L_{nt}}$ for both ideal and real cases. The controller calculates the required center current $\overline{i_{\mathrm{DC}}}$ based on the measured capacitor voltage and output inductor current, adjusting the phase shift to ensure a smooth transient, following

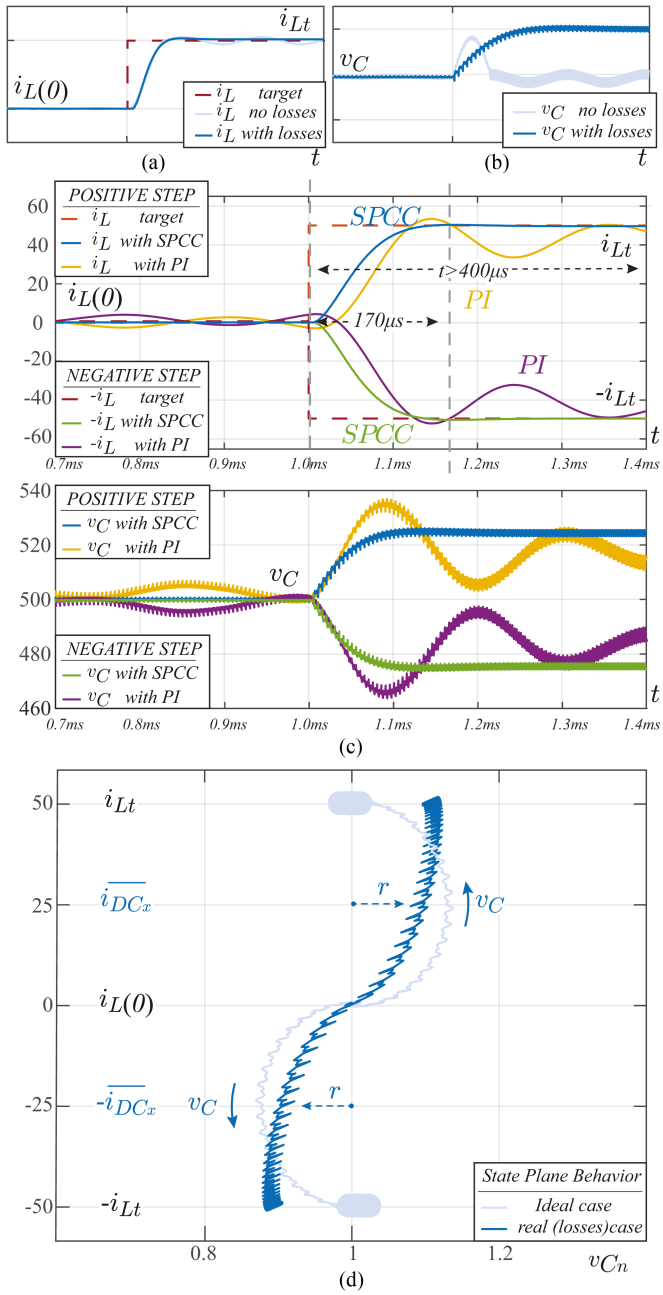

Fig. 9. Simulation results of the state-plane centric control. Comparison between the ideal case with no losses and the real case with losses for (a) i_L and (b) v_C. (c) Comparison between the state-plane centric control and the PI in charging and discharging modes in terms of i_L and v_C. (d) State-plane analysis in the ideal and the real case.

a unique circular trajectory to reach the target. Output losses cause minor voltage deviations and slight shifts in the final value, (4.4% of the battery voltage). The state-plane domain simulation, shown in Fig. 9(d), highlights how $\overline{i_{\mathrm{DC}}}$ is calculated once in the ideal case, resulting in a perfect circular trajectory. In the real case, accounting for compensated output losses, the trajectory deviates from a circle due to the unmodeled dynamics and the continuous update of the value of d. To evaluate the dynamic performance of the proposed state-plane centric control, a comparison was made with a traditional proportional integral

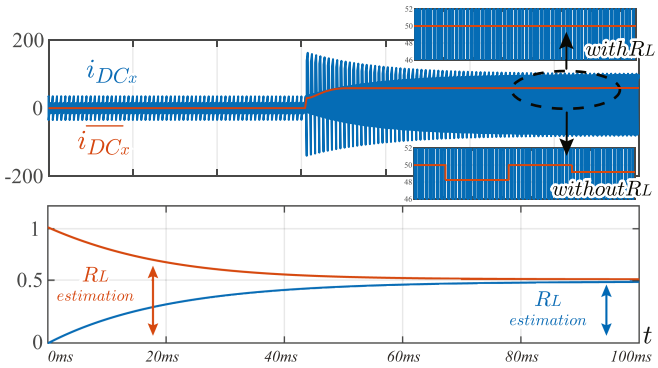

Fig. 10. Output losses estimation and i_{DC} with and without the compensator and with initial error in the losses estimation.

TABLE I
SIMULATION AND EXPERIMENTAL PLATFORM PARAMETERS

PARAMETER	SIM. VALUES	EXP. VALUES
f_{sw}	200 kHz	
L_{lk}	10 μH	6.8 μH
L	10 μH	
C	100 μF	96 μF
n	1/1	1/1.67
V_{in}	800 V	60 V
V_{batt}	500 V	42 V
I_{L_t}	$\pm$50 A	$\pm$2 A
P_{out}	25 kW	85 W

(PI) controller, as shown in Fig. 9(c). The results demonstrate that the proposed controller solves large transients faster and more predictably than the linear controller, with no overshoot or spikes, minimizing battery stress and voltage fluctuations, lowering battery stress. The proposed controller reaches the final value in just 170 μs, accurately setting the current and phase shift without inducing oscillations, and the new voltage value, due to the losses, is set at 525 V. The integral action is crucial during the charging mode, as any rapid fluctuation in current can damage the battery and compromise its lifespan. In comparison, under the same conditions, the PI controller, tuned to have the values of $k_p = 0.425$ and $k_i = 26.4$, results in a $10\%-20\%$ overshoot in the output current, as well as a first overshoot of 10 V for the output voltage, and takes 0.8 ms to reach the target. Fig. 10 illustrates the differences between the compensated and uncompensated systems. Specifically, estimating the output losses R_L with an integral constant $K_{int} = 10^{-4}$, which in the simulations are set to 0.5 Ω, stabilizes the rectified current on the secondary side, and consequently, the target value of i_L over the long term. This approach prevents further displacement of i_{DC} and avoids leaving the linear region unless a new step change occurs. Fig. 11 shows simulation results of the state-plane centric control with the largest transient possible, starting from the maximum discharging current of $i_L = -50$ A and reaching the maximum charging current of $i_L = 50$ A. In this case, the controller calculates the center of the circular trajectory, and due to the large transient, the jump into the final linear region is the

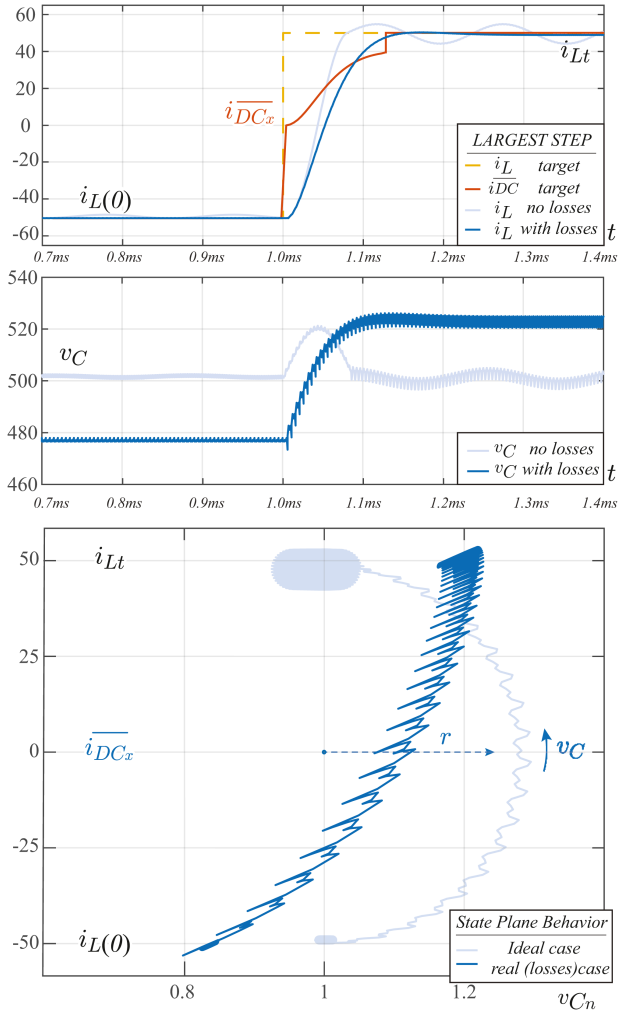

Fig. 11. Simulation results of the state-plane centric control in terms of i_L v_C in the ideal and real cases with the largest transient possible.

10% of the total transient, so from 40 to 50 A, the value of $\overline{i_{DC}}$ shows a step to achieve the maximum current.

Since the control decisions are geometry-based and the controller's action depends on the output tank's LC parameters, a mismatch in the normalizing time does not affect the dynamic behavior. Deviations in the characteristic impedance cause the trajectories to deviate from ideal circular paths. To illustrate this, Fig. 12 presents transient response simulations of the proposed state-plane centric control, considering uncertainties of $\pm 20\%$ in the output parameters. As observed, the trajectories that deviate the most from the standard case (i.e., when the controller is designed for $L = 10$ μH and $C = 100$ μF) are those where the parameter deviations have opposite signs, maximizing variations in the output characteristic impedance. This analysis highlights the robustness of the proposed state-plane centric control, which effectively handles large parameter variations while maintaining a reliable and predictable response with only minor dynamic deviations from the standard case. To evaluate the robustness of the proposed method against errors in loss estimation, simulations were performed with deviations in the estimated losses. Even with an error in the initial estimated resistance value (see

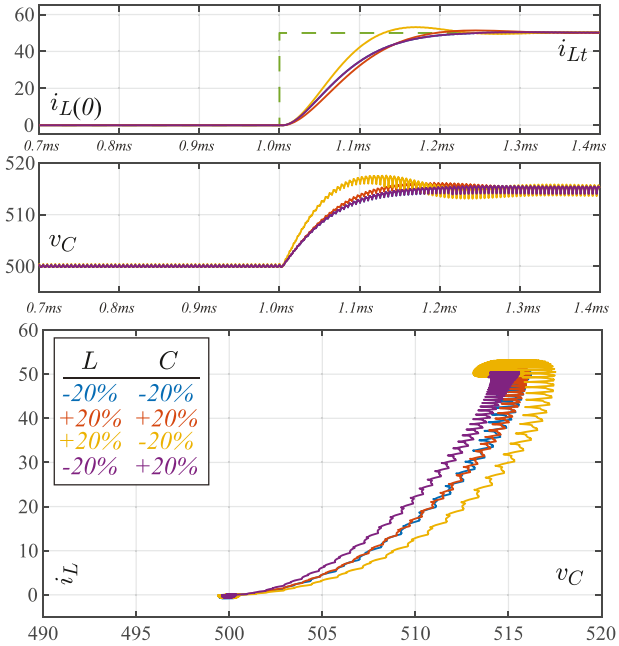

Fig. 12. Dynamic response of the DAB converter controlled with the state-plane centric control for an *LC* parameter variation of ±20%.

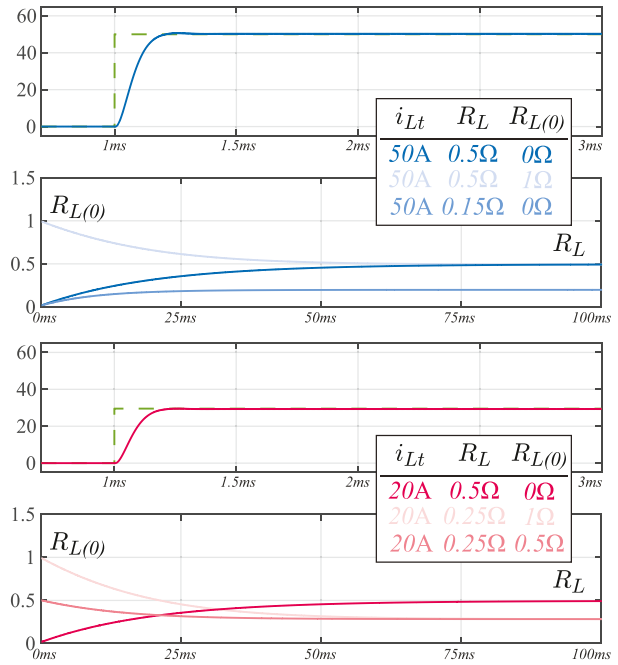

Fig. 13. Simulation results of the losses compensator using different values of R_L, $R_L(0)$, and i_{L_t}.

Fig. 13), the controller converges to the correct operating point, even considering two different targets $i_{L_t} = 50$ and $i_{L_t} = 20$. This demonstrates that while loss estimation influences steady-state accuracy, it does not affect the large transient response.

V. Experimental Results

A DAB hardware platform featuring an industry-standard TI-C2000 Series microcontroller was developed using the

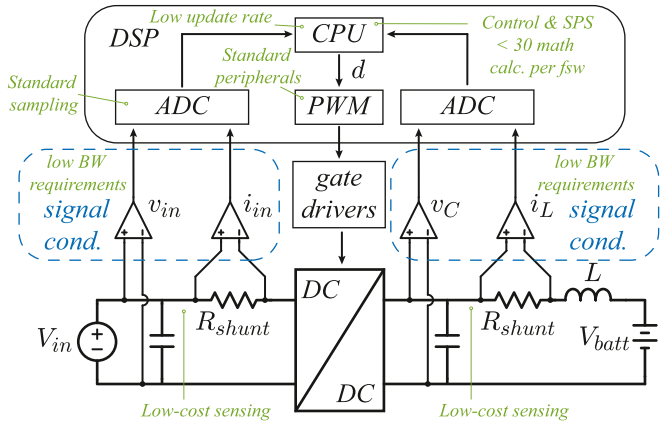

Fig. 14. State-plane centric control low-cost implementation with a battery and TI C2000 microcontroller.

parameters detailed in Table I and a hardware implementation diagram is shown in Fig. 14. The sensors used to measure the input and output current, input and output voltage, and transformer current consist of a combination of low-cost voltage dividers, 50-mΩ shunt resistors, and classical signal conditioning via op-amps with a sensing bandwidth of 1.3 MHz for the current and 1 MHz for the voltage, which is sufficient to capture the relevant converter dynamics and ensure reliable per-cycle control updates to route the signals to the microcontroller's ADC stages. The $\overline{i_{\mathrm{DC}}}$ and phase-shift calculations are performed every PWM cycle, enabling a fast response to sudden reference changes. The power factor correction (PFC) stage is emulated using a programmable power supply with bidirectional power flow capability, while a 12S4P battery pack (42 V and 12 Ah) is used as the load on the secondary side. This platform supports full bidirectional conversion thanks to the resistor in parallel to the power supply. The overall power of the converter is limited by the capabilities of the power supply and the battery, so the parameters were selected to replicate DAB behavior while limiting power to 85 W. Fig. 6(b) displays the simulated waveforms of the primary and secondary transformers voltages v_p and v_s, as well as the leakage inductor current $i_{L_{\mathrm{lk}}}$, and Fig. 7 shows the same waveforms and the rectified current i_{DC} in open loop; this is last shown because its average value is the key parameter for the proposed control. In this case, the primary-side transformer voltage ranges from −60 to 60 V, while the secondary side ranges from −50 to 50 V.

The switching frequency is set to 200 kHz. The captures Figs. 15, 16, and 17 show the effect of the change in phase shift d on the rectified current i_{DC}. Fig. 15 shows the experimental results for a positive output current step of $\Delta i_L = 2A$. During this step, both the value of $\overline{i_{\mathrm{DC}}}$ and the phase shift d change every switching cycle. Initially, the average current starts from $i_{\mathrm{DC}} = 0$ and quickly reaches the center of the average natural trajectory. Due to losses, the initial and the final values of v_C are different. However, once the phase-shift value is aligned with the center of the circular trajectory defined by the parameters i_L and v_C, $\overline{i_{\mathrm{DC}}}$ gradually increases each PWM cycle until it reaches its final value, and d adjusts accordingly, also updating once per PWM cycle. At this point, the final values of d and

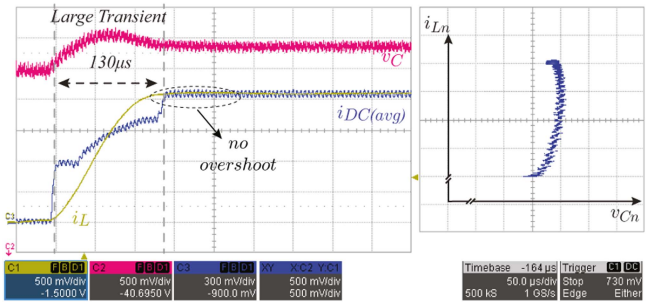

Fig. 15. Experimental results of the state-plane centric control in the time domain and state-plane behavior in terms of i_L and v_C in charging mode with a positive step current of $2A$.

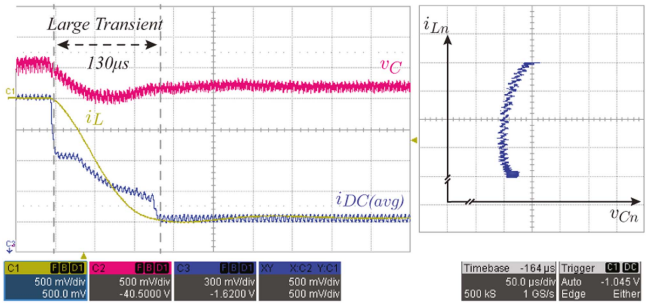

Fig. 16. Experimental results of the state plane in the time domain and state-plane behavior in terms of i_L and v_C in discharging mode with a negative step current of $-2A$.

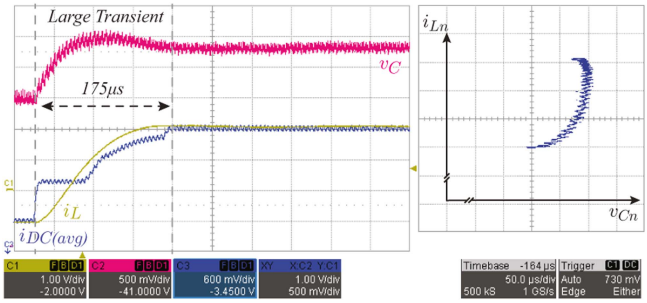

Fig. 17. Experimental results of the state plane in the time domain and state-plane behavior in terms of i_L and v_C in with a current step from -1 to 2 A.

i_L are maintained. The control action achieves the target in just 130 μs. The control variable i_{DC} is output to confirm that its behavior matches the simulation. The results demonstrate a fast, predictable transient response, avoiding current spikes in the battery and limiting overshoot in the capacitor voltage. This highlights the advantage of the proposed control over traditional small-signal-based methods considering that it was implemented on a low-cost TI C2000 series microcontroller using standard peripherals, demonstrating the feasibility of deploying this control in resource-constrained environments. Fig. 16 shows similar behavior in discharging mode, emulating a V2X scenario where the EV battery supplies power to buildings or supporting the grid.

A negative output current step of $\Delta i_L = -2A$ is applied, and the control variables behave similarly to the charging scenario.

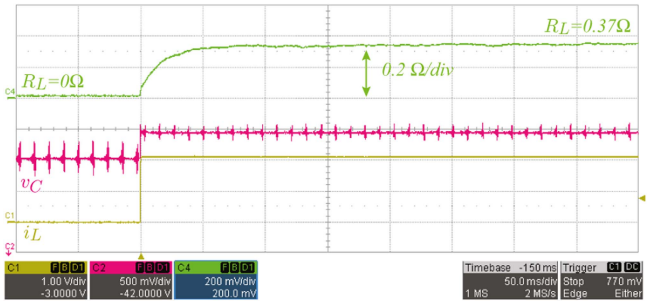

Fig. 18. Experimental results of the state plane in the time domain considering the losses estimation R_L achieving a final value of 0.37 Ω.

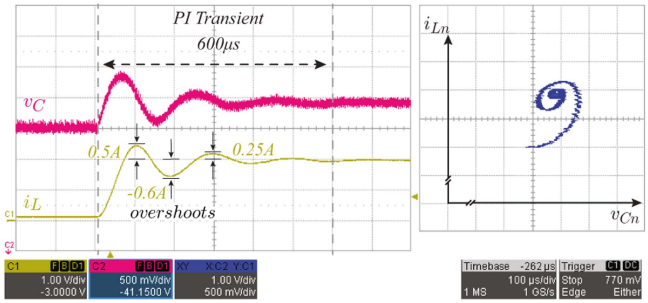

Fig. 19. Experimental results of the same DAB converter controlled by a PI in terms of i_L and v_C in time domain and XY behavior.

In this case, both the output current and capacitor voltage steps are negative, driving a counterclockwise circular trajectory in the XY plot. Even using a negative current step, the proposed controller maintain its main advantage of a predictable transient behavior, with zero overshoot thanks to the ability to remain in the final linear region, which is set to be the 10% of the overall transient. This stability in both charging and discharging modes demonstrates the controller's ability to adapt quickly to dynamic changes in the system's environment. Fig. 17 demonstrates the converter's ability to handle a step from a negative value of -1 A to a positive value of 2 A and solving it in 175 μs, showcasing the controller capability to respond rapidly not only in charging or discharging modes but also in managing the large transients, also in this case, with no overshoot Fig. 18 shows the state-plane centric control combined with the loss estimator algorithm in the time domain. The resistance estimation is performed with a slow integrator, where $K_{\text{int}} = 10^{-5}$ is used. A digital-to-analog converter output from the microcontroller was used to display the variable R_L, which stabilizes at 0.37 Ω after 150 ms, ensuring stable control in steady state. Fig. 19 compares the same converter controlled with a well-tuned PI controller in charging mode. While the PI controller reaches the target in 600 μs, making it five times slower than the state-plane centric control, it also introduces two overshoots in the current i_L and voltage v_C. This validation further reinforces the state-plane centric control as a good alternative of the traditional PI control. As shown in Fig. 19, the PI-controlled DAB exhibits an initial overshoot followed by damped oscillations before arriving at the target point. In contrast, the state-plane centric control smoothly follows a circular trajectory without overshoot or oscillations, reaching

steady-state faster. In addition, Figs. 16 and 17 highlight the robustness of the state-plane centric control to parameter variations. These findings confirm that the proposed method provides an efficient and stable solution for DAB control in V2X applications. Experimental results confirm that the controller has an ultrafast transient response and maintains stable operation even with the presence of output losses. The controller successfully adjusts for loss estimation errors over time, preventing steady-state errors and deviations from the target point. The integral loss estimator gradually corrects any steady-state mismatches, demonstrating the controller's robustness in practical applications.

VI. Conclusion

This article introduced a high-performance fast state-plane centric control for DAB converters performed using average state equations and representing them in the state-plane domain. An average large-signal model of the DAB converter with single-phase-shift modulation and an output LC filter connected to a battery was derived to describe the converter dynamics. The state-plane analysis revealed that the desired operating point can be reached by following a unique circular trajectory starting from any initial condition, achieving an ultrafast and predictable large transient response, capable of achieving the maximum power rating in less than 0.5 ms. Compared to traditional PI control, the state-plane centric control reduces transient response, eliminates overshoot, and provides a computationally efficient solution and unlike other nonlinear control techniques, the proposed method is compatible with industry-standard hardware and can be easily implemented in both low- and high-power DAB converters. Moreover, the proposed state-plane centric control can be readily adapted to various converter parameters, including input and output voltages that match common battery and rectifier dc bus levels or high-power transformers. This adaptability extends the potential applications of the proposed solution across a wide range of EV chargers and the implementation using a standard TI C2000 microcontroller underscores the simplicity of the control introduced. The effectiveness of the detailed control is demonstrated through mathematical expressions and validated by both simulation and experimental results using a DAB converter platform, with a power supply emulating the active front end on the primary side and a 42-V battery on the secondary side to emulate a scaled down battery charger.

References

[1] V. M. Iyer, S. Gulur, and S. Bhattacharya, "Small-signal stability assessment and active stabilization of a bidirectional battery charger," *IEEE Trans. Ind. Appl.*, vol. 55, no. 1, pp. 563–574, Jan./Feb. 2019.

[2] T. Liu et al., "Design and implementation of high efficiency control scheme of dual active bridge based 10 kV/1 MW solid state transformer for PV application," *IEEE Trans. Power Electron.*, vol. 34, no. 5, pp. 4223–4238, May 2019.

[3] R. Chen et al., "Analysis and design for medium voltage dual active bridge converter based on series-connected SiC MOSFETs," *IEEE Trans. Power Electron.*, vol. 38, no. 12, pp. 15620–15633, Dec. 2023.

[4] M. Kheraluwala, R. Gascoigne, D. Divan, and E. Baumann, "Performance characterization of a high-power dual active bridge DC-to-DC converter," *IEEE Trans. Ind. Appl.*, vol. 28, no. 6, pp. 1294–1301, Nov./Dec. 1992.

[5] F. Krismer and J. W. Kolar, "Efficiency-optimized high-current dual active bridge converter for automotive applications," *IEEE Trans. Ind. Electron.*, vol. 59, no. 7, pp. 2745–2760, Jul. 2012.

[6] A. R. Rodríguez Alonso, J. Sebastian, D. G. Lamar, M. M. Hernando, and A. Vazquez, "An overall study of a dual active bridge for bidirectional DC/DC conversion," in *Proc. IEEE Energy Convers. Congr. Expo.*, 2010, pp. 1129–1135.

[7] B. Zhao, Q. Song, W. Liu, and Y. Sun, "Overview of dual-active-bridge isolated bidirectional DC–DC converter for high-frequency-link power-conversion system," *IEEE Trans. Power Electron.*, vol. 29, no. 8, pp. 4091–4106, Aug. 2014.

[8] D. Lyu, C. Straathof, T. B. Soeiro, Z. Qin, and P. Bauer, "ZVS-optimized constant and variable switching frequency modulation schemes for dual active bridge converters," *IEEE Open J. Power Electron.*, vol. 4, pp. 801–816, 2023.

[9] N. H. Baars, J. Everts, C. G. E. Wijnands, and E. A. Lomonova, "Performance evaluation of a three-phase dual active bridge DC–DC converter with different transformer winding configurations," *IEEE Trans. Power Electron.*, vol. 31, no. 10, pp. 6814–6823, Oct. 2016.

[10] J. Huang, Z. Li, L. Shi, Y. Wang, and J. Zhu, "Optimized modulation and dynamic control of a three-phase dual active bridge converter with variable duty cycles," *IEEE Trans. Power Electron.*, vol. 34, no. 3, pp. 2856–2873, Mar. 2019.

[11] Z. M. Dalala, Z. U. Zahid, O. S. Saadeh, and J.-S. Lai, "Modeling and controller design of a bidirectional resonant converter battery charger," *IEEE Access*, vol. 6, pp. 23338–23350, 2018.

[12] A. Filba-Martinez, S. Busquets-Monge, J. Nicolas-Apruzzese, and J. Bordonau, "Operating principle and performance optimization of a three-level NPC dual-active-bridge DC–DC converter," *IEEE Trans. Ind. Electron.*, vol. 63, no. 2, pp. 678–690, Feb. 2016.

[13] F. Zhang, Y. Ren, X. Yang, W. Chen, and H. Wu, "Capacitor voltage balancing control for a novel 5-level dual active bridge converter," *IEEE Trans. Power Electron.*, vol. 37, no. 12, pp. 14738–14754, Dec. 2022.

[14] Z. Ji, Q. Wang, D. Li, and Y. Sun, "Fast DC-bias current control of dual active bridge converters with feedforward compensation," *IEEE Trans. Circuits Syst. II, Exp. Briefs*, vol. 67, no. 11, pp. 2587–2591, Nov. 2020.

[15] P. F. S. Costa, P. H. B. Löbler, L. Roggia, and L. Schuch, "Modeling and control of DAB converter applied to batteries charging," *IEEE Trans. Energy Convers.*, vol. 37, no. 1, pp. 175–184, Mar. 2022.

[16] Y.-C. Jeung and D.-C. Lee, "Voltage and current regulations of bidirectional isolated dual-active-bridge DC–DC converters based on a double-integral sliding mode control," *IEEE Trans. Power Electron.*, vol. 34, no. 7, pp. 6937–6946, Jul. 2019.

[17] A. Dòria-Cerezo, F. M. Serra, F. D. Esteban, D. Biel, and R. Griñó, "Comparison of first- and second-order sliding-mode controllers for a DC-DC dual active bridge," *IEEE Access*, vol. 10, pp. 40264–40272, 2022.

[18] M. Cupelli et al., "Port controlled hamiltonian modeling and IDA-PBC control of dual active bridge converters for DC microgrids," *IEEE Trans. Ind. Electron.*, vol. 66, no. 11, pp. 9065–9075, Nov. 2019.

[19] L. Tarisciotti, L. Chen, S. Shao, T. Dragičević, P. Wheeler, and P. Zanchetta, "Finite control set model predictive control for dual active bridge converter," *IEEE Trans. Ind. Appl.*, vol. 58, no. 2, pp. 2155–2165, Mar./Apr. 2022.

[20] Y. Zhu et al., "Model predictive control with a novel parameter identification scheme for dual-active-bridge converters," *IEEE Trans. Emerg. Sel. Topics Power Electron.*, vol. 11, no. 5, pp. 4704–4713, Oct. 2023.

[21] S. M. Akbar, A. Hasan, A. J. Watson, and P. Wheeler, "Model predictive control with triple phase shift modulation for a dual active bridge DC-DC converter," *IEEE Access*, vol. 9, pp. 98603–98614, 2021.

[22] G. G. Oggier and M. Ordonez, "High-efficiency DAB converter using switching sequences and burst mode," *IEEE Trans. Power Electron.*, vol. 31, no. 3, pp. 2069–2082, Mar. 2016.

[23] P. Xu et al., "Large-signal stability for DAB converters feeding constant power load based on state trajectory analysis," *IEEE Trans. Transport. Electrific.*, vol. 11, no. 1, pp. 3244–3261, Feb. 2025.

[24] Z. Xiao, Z. Yao, F. Deng, Y. Zhang, and Y. Tang, "Exploring the extreme dynamic transition response of dual active bridge converters," *IEEE Trans. Power Electron.*, vol. 40, no. 5, pp. 6988–7001, May 2025.

[25] J. Hu, S. Cui, and R. W. De Doncker, "Closed-loop black start-up of dual-active-bridge converter with boosted dynamics and soft-switching operation," *IEEE Trans. Power Electron.*, vol. 36, no. 10, pp. 11009–11013, Oct. 2021.

[26] I. Galiano Zurbriggen, M. Ordonez, and M. Anun, "PWM-geometric modeling and centric control of basic DC–DC topologies for sleek and reliable large-signal response," *IEEE Trans. Ind. Electron.*, vol. 62, no. 4, pp. 2297–2308, Apr. 2015.

[27] N. A. Meineri, I. Santana, and I. G. Zurbriggen, "Ultra-fast MPPT for residential PV systems with low DC-link capacitance and differential power processing," *IEEE Trans. Power Electron.*, vol. 40, no. 2, pp. 2736–2745, Feb. 2025.

[28] I. Galiano Zurbriggen, F. Degioanni, and M. Ordonez, "Near-time-optimal dynamics in PWM DC–DC converters: Dual-loop geometric control," *IEEE Trans. Emerg. Sel. Topics Power Electron.*, vol. 9, no. 1, pp. 167–182, Feb. 2021.

[29] M. Sposito, N. A. Meineri, I. Santana, and I. G. Zurbriggen, "State-plane control of DAB-based battery chargers," in *Proc. IEEE Energy Convers. Congr. Expo.*, 2024, pp. 4670–4675.

Matteo Sposito (Graduate Student Member, IEEE) was born in Milano, Italy. He received the B.Sc. and M.Sc. degrees in automation and control engineering from the Politecnico di Milano, Milano, in 2017 and 2019, respectively. He is currently working toward the Ph.D. degree in electrical and computer engineering with the University of Calgary, Calgary, AB, Canada.

In 2021, he Cofounded the innovative start-up ePEBBs Srl. His research interests include the development of linear, nonlinear, and hybrid control strategies for bidirectional isolated power electronic converters.

Ignacio Galiano Zurbriggen (Member, IEEE) was born in San Francisco, Cordoba, Argentina. He received the M.A.Sc. and Ph.D. degrees in electrical and computer engineering from the University of British Columbia (UBC), Vancouver, BC, Canada, in 2013 and 2020, respectively, and the Ingeniero degree in electronics engineering from the National University of Cordoba, Cordoba, in 2010.

He is currently an Assistant Professor with the School of Sustainable Energy Engineering, Simon Fraser University, Burnaby, BC, and an Adjunct Professor with the Electrical and Software Engineering Department, University of Calgary, Calgary, AB, Canada. His work in power electronics includes industrial research and development experience with Tesla and Computrol. His research interests include the study of power electronic converters as technology-enabling building blocks for applications in sustainable energy and transportation.

Dr. Zurbriggen has delivered multiple IEEE technical presentations and seminars and serves as an Associate Editor for IEEE OPEN JOURNAL OF POWER ELECTRONICS, as well as a Reviewer for several IEEE journals and conferences.